INTERFACE

royalsocietypublishing.org/journal/rsif

Research

Cite this article: Krsmanovic M, Ali H, Biswas D, Ghosh R, Dickerson AK. 2022 Fouling of mammalian hair fibres exposed to a titanium dioxide colloidal suspension. *J. R. Soc. Interface* **19**: 20210904.
https://doi.org/10.1098/rsif.2021.0904

Received: 1 December 2021
Accepted: 16 March 2022

Subject Category:
Life Sciences–Engineering interface

Subject Areas:
biomechanics, biotechnology, chemical biology

Keywords:
flow, particle deposition, manufactured filaments, fur cleaning, surface interactions

Author for correspondence:
Andrew K. Dickerson
e-mail: ad@utk.edu

Electronic supplementary material is available online at https://doi.org/10.6084/m9.figshare.c.5912842.

THE ROYAL SOCIETY PUBLISHING

Fouling of mammalian hair fibres exposed to a titanium dioxide colloidal suspension

Milos Krsmanovic[1], Hessein Ali[2], Dipankar Biswas[3], Ranajay Ghosh[1] and Andrew K. Dickerson[4]

[1]Department of Mechanical and Aerospace Engineering, University of Central Florida, Orlando, FL, USA
[2]Department of Mechanical Engineering, Union College, Schenectady, NY, USA
[3]School of Medicine, Johns Hopkins University, Baltimore, MD, USA
[4]Department of Mechanical, Aerospace, and Biomedical Engineering, University of Tennessee, Knoxville, TN, USA

MK, 0000-0003-1346-3672; AKD, 0000-0003-1220-1048

Fouling of surfaces in prolonged contact with liquid often leads to detrimental alteration of material properties and performance. A wide range of factors which include mass transport, surface properties and surface interactions dictate whether foulants are able to adhere to a surface. Passive means of foulant rejection, such as the microscopic patterns, have been known to develop in nature. In this work, we investigate the anti-fouling behaviour of animal fur and its apparent passive resistance to fouling. We compare the fouling performance of several categories of natural and manufactured fibres, and present correlations between contamination susceptibility and physio-mechanical properties of the fibre and its environment. Lastly, we present a correlation between the fouling intensity of a fibre and the cumulative impact of multiple interacting factors declared in the form of a dimensionless group. Artificial and natural hair strands exhibit comparable anti-fouling behaviour in flow, however, the absence of flow improves the performance of some artificial fibres. Among the plethora of factors affecting the fouling of fur hair, the dimensionless groups we present herein provide the best demarcation between fibres of different origin.

1. Introduction

Submerged or frequently wetted surfaces are susceptible to rapid accumulation of foreign matter in a process known as fouling. Fouling can be caused by inorganic matter [1], non-living organic matter [2] or living matter as is the case with biofouling. Fouling is a widespread phenomenon, present in a variety of industries and engineered systems: potable water supply [3,4], waste water treatment [5], medical devices [6,7], dental care [8], food processing [9], marine transport [10], and heat transfer devices [11], to mention but a few. Fouling is predominately adverse, impacting the performance, cost, and reliability of fouled systems and processes [11,12], although fouling can provide practical benefits in limited cases [13,14].

The fouling process is influenced by a large number of factors: physico-chemical, mechanical, and stochastic factors, temporal changes, and in case of biofouling, genotypic factors and deterministic phenomena [15]. The particle deposition rate onto a submerged stratum is impacted by a particle's shape and orientation [16], inertial force of the particle, gravity, Brownian and turbulent diffusion [17], particle size, substrate topography, surface interactions such as van der Waals forces, electrostatic double-layer forces and other charge-related interaction forces [11]. Adhesion depends on colloidal behaviour of particles, and inorganic particles larger than approximately 1 m will be carried away from the surface by gravity or momentum. Larger contact area, available to non-spherical particles or particles matching the size of the surface roughness features, increases particle retention. Other surface interaction phenomena may exist depending on the environmental conditions, such as the electrostatic double-layer repulsion in high pH liquids. The probability of detachment is related to conditions within

the laminar boundary layer. Viscous flow, Brownian motion and hydrodynamic stresses determine whether pivotal movement and lifting forces necessary to remove the particle can overcome attractive forces [11]. An extensive review of flow and topography governance over the inorganic fouling process can be found in Melo *et. al* [11] and the biofouling process in Krsmanovic *et. al* [18].

A variety of active and passive measures have been developed to counteract the impact of fouling [19–23]. In nature, compounds produced by marine microorganisms have been shown to possess anti-fouling properties [24,25]. Investigation of terrestrial mammal fur demonstrated similar resistance to biofouling [26]. It has been noted, however, that semi-aquatic mammals' grooming habits serve the maintenance of the insulating layer of trapped air in the fur, rather than the removal of foulants [27]. Only several anecdotal observations of foulant growth on semi-aquatic mammals have been made in case of wild sea otters or polar bears monitored in environments with elevated temperatures [28–31]. Fur does not release toxins, and is neither superhydrophobic nor superhydrophilic [32]. Therefore, some other passive anti-fouling mechanisms appear to be critical for furry mammal's ability to remain clean. However, the physical mechanisms underlying fur's resistance to foulants is largely unknown. Gaining insight into the intricacies of the passive anti-fouling defences of fur could enable mimicry within manufactured structures that are chemical-free and do not rely on coatings needing replenishment.

As a part of a broader effort to investigate the ability of passive, physiological properties of fur—surface structure, deformation and aggregate behaviour—to resist fouling, we expose animal and artificial fibres to liquid flow rich in inorganic fouling particles. Flow is an apparent critical factor for success of a fouling process as static environments both reduce the chance of foulant encounters with the stratum [33–37], and the rate of bio-foulants' proliferation once the attachment occurs [38,39]. Another physiological factor, surface features—characterized by overall roughness—critically affects the ability of a substrate to arrest or release a particle [39–43]. Surface interactions, foremost driven by the surface free energy, dictate the probability of initiation of the fouling process [44–50]. For a given liquid and surface topography, surface interactions are driven by the choice of the stratum material. We compare the combined impact of several critical factors—flow, surface topology and surface topography—on the success of the fouling process across several types of fibres, representing different materials and surface topographies. We present our experimental methods in §2, our results in §3, a dimensional analysis of our results is given in §4, and our work is discussed in §5.

2. Material and experimental methods

2.1. Materials

Six furs are selected to represent both semi-aquatic and terrestrial mammal orders: American beaver (*Castor canadensis*), muskrat (*Ondatra zibethicus*), sea otter (*Enhydra lutris*), coyote (*Canis latrans*), springbok (*Antidorcas marsupialis*) and muskox (*Ovibos moschatus*). The orders are selected to represent various natural habitats and a range of body masses spanning two orders of magnitude, who together influence the necessity for—and the ability of—an animal to dry itself [51]. While nearly all animal pelts used in experimentation are tanned, no distinguishable structural changes of hair surfaces is observed. The strands are harvested using stainless steel forceps and disposable carbon steel surgical blades. The follicles are manipulated delicately to minimize the strain, contamination, or other alteration of physical properties. In the case of species whose fur is comprised of guard hair and underfur, guard hair is used. Cross-sections are prepared for SEM imaging using epoxy compound coating (Marine-Tex) which maintained the fur strand shape intact as it is sheared on a polisher (Allied High Tech Products). An overview of the fibre surface topographies and cross-sections has been provided in figure 1.

An 80 µm thick polypropylene (PP) monofilament fibre (Textile Development Associates, Inc.), comparable in diameter to those of the selected natural fibres, is employed as a control. The same type of fibre, coated with stock liquid latex is used as a second control. Latex is chosen based on the substantial susceptibility to biological fouling [52]. The PP strand is coated by repeated rapid submersion in liquid latex, which allowed formation of a relatively thin and uniform coating, approximately 500 µm thick. Additional latex flat coupons, approximately 2.1×4.6 mm in size and 0.25 mm thick, are used to asses the deposition of particles on a flat surface located in the liquid.

A suspension of titanium dioxide (TiO_2) in distilled water is selected as our experimental fouler based on the authors' previous work [53], where fouling of the flow system is observed as a side-effect of TiO_2 use. Foulant deposition in flow systems with TiO_2 concentrations as low as 0.2 mg l^{-1} is observable by the naked eye in less than an hour. Conduits take on the appearance of fine particulate, cloudy deposition. This experiment used a suspension with TiO_2 concentration of 0.4 mg l^{-1}. Viscosity measurements of the TiO_2 suspension is carried out using the spindle type viscometer (Brookefield, model LV). Constant dynamic viscosity of $\mu = 0.94 \pm 0.02$ cP is measured for several different shear rates, indicating that the suspension is Newtonian.

The number of particles in suspensions with different concentrations of TiO_2 is determined using a spectrophotometer (BIO-RAD, model SmartSpec Plus) and a Neubauer double cell 0.1 mm haemocytometer (EMS). Optical density measurements at a wavelength of 600 nm (OD_{600}) have been carried out for 15 samples with different TiO_2 concentrations. Optical density OD_{600} proved the most suitable for the whole range of measured values in the preliminary tests. The number of particles per unit volume of the suspension is counted for the same samples using the haemocytometer, which allowed the establishment of the second degree polynomial curve fit

$$N = -0.0186 \cdot OD_{600}^2 + 0.1169 \cdot OD_{600} + 0.0009, \qquad (2.1)$$

where N is the number of particles per millilitre of water. The method used to form equation (2.1) is provided in electronic supplementary material, figure S1.

The TiO_2 manufacturer (Pantai USA) specifies that the dry TiO_2 powder has 0.05% residues on a 45 µm sieve, measured as per ISO 787-18 standard [54]. The specified sieved material size is approximately O(2) larger compared to the particle diameter of the conventional TiO_2 nanoparticle [55–58]. To determine the particulate aggreagtion size distribution in suspension, we sampled liquid from the experimental flow system–described in §2.2–running for 12 h. Three 0.2 mm

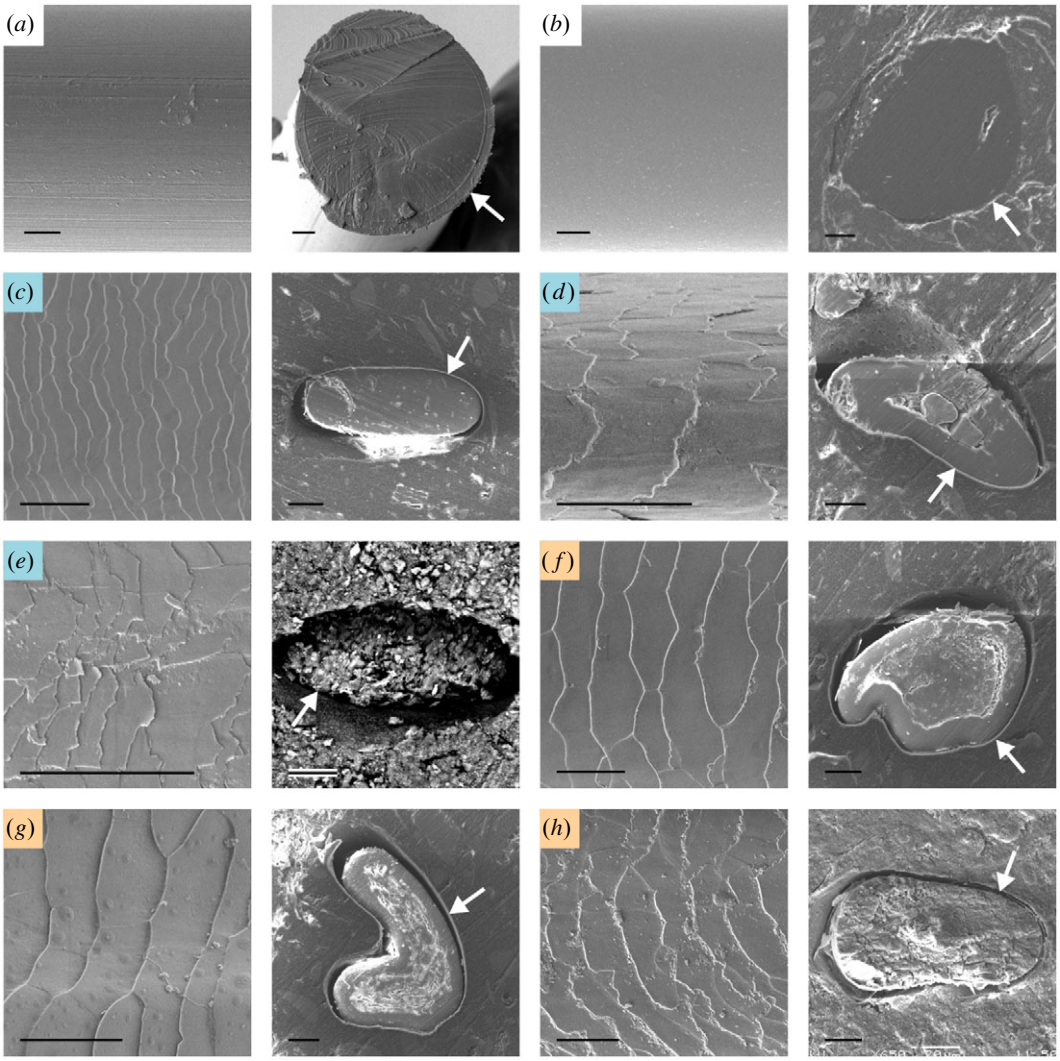

Figure 1. SEM images of fibre surface topographies and cross-sections. A pair of panels depicts a side view and a cross-sectional view. (*a–b*) Synthetic fibres: (*a*) polypropylene monofilament, (*b*) latex coated polypropylene monofilament. (*c–e*) Semi-aquatic mammals: (*c*) American beaver, (*d*) muskrat, (*e*) sea otter. (*f –h*) Terrestrial mammals: (*f*) coyote, (*g*) springbok, (*h*) muskox. Arrows indicate fibre boundaries. Scale bars represent 20 µm.

samples are observed under the microscope (Keyence, model VHX-900), using glass cover slides and cover slips (AmScope). Microscope images are processed using FIJI imaging software to identify the clustered TiO_2 particles. Approximately 74% of clumps have a projected area of $\leq 5\ \mu m^2$. Clump sizing methodology and the frequency of clump sizes, as measured by projected area, are shown in electronic supplementary material, figures S2 and S3.

2.2. Flow system

Fur fibres are held in the liquid stream using a custom made mount. The hair mount (1), shown in figure 2 inset, is designed to serve a dual purpose of sample support and as the conduit connector. We note in §1 that the velocity field critically influences fouling. An efficient fur mount design allows testing of fibres in both laminar flow and near-stagnant liquid. Manufactured polylactide (PLA) connectors are designed to achieve a smooth transition from a circular to rectangular conduit, thus minimizing the flow disruption. Smooth expansion and contraction allows for formation of corner zones where the flow is near-stagnant. One of the two connectors is made with four 0.25 mm deep indentations on the contact face to accommodate four fibre samples (*inset*). The fibres are aligned in the same plane, all perpendicular to the flow, in order to avoid the wake effects from other strands. An additional connector variant is made with a coupon-shaped indentation in the zone where the flow is nearly stagnant (*inset*). Test samples are held in place using UV-activated adhesive (RapidFix) so there is no adhesive contamination of samples' wet surfaces. The adhesive affixes the two connector halves, and acts as a sealant. The hair mount is mounted vertically to the backboard with straight conduit runs up- and downstream, as shown in figure 2. Omission of elbows at the pump's discharge together with zip-tie anchors holding the mount in vertical position minimizes periodic displacement of the mount during pumping.

Buffer reservoirs adapted from stock plastic containers, shown in figure 2 (2), are kept on magnetic stirrers (3) (Chemglass Life Sciences, model OptiCHEM) set to maintain a rotation of approximately 300 revolutions per minute. The buffers are used to absorb potential hydraulic anomalies in the displacement volume pumping system, to provide additional liquid volume in case of liquid loss, and to ensure proper mixing of the TiO_2 particles in the suspension. The total volume of liquid in each system is approximately 150 mm. After each filling, the reservoirs are covered to minimize evaporation. The flow system operates at room

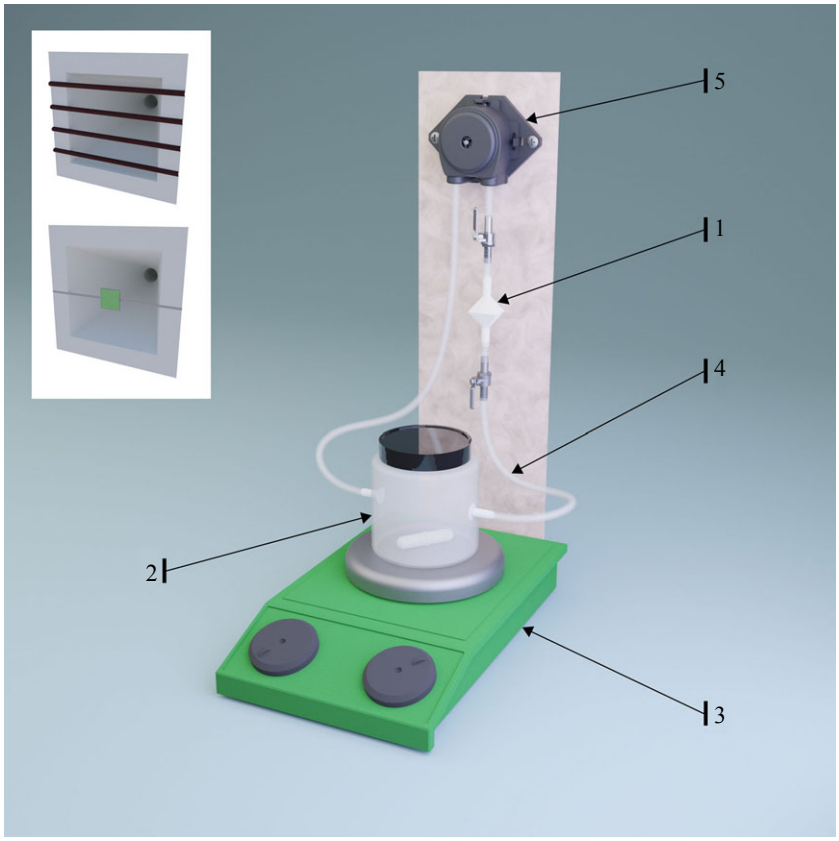

Figure 2. Experimental flow system. The inset shows the details of fur and coupons mounting connectors. (1) Fur mounting connectors, (2) reservoir, (3) magnetic stirring plate, (4) tubing and (5) peristaltic pump.

temperature of 23°C, and the stirrer plate reaches a maximum temperature of 26°C during the operation due to stirring. All elements of the system are connected by flexible conduits (4): vinyl main flow lines, and food grade silicone tubes in the pump. Large radius tube paths are used to reduce the pressure drop and the chance of excessive TiO_2 deposition.

Peristaltic pumps (5) (GOSO and Atlas Scientific) maintain the foulant stream circulation in the flow system, and are chosen because they contain no parts in contact with the foulant stream. Pump speed is controlled either by a programmable controller (Arduino, model UNO) or directly by varying the supply voltage from a bench-top DC power supply (Yescom, model DCP305D). The flow rate is set to 40 ml min^{-1}. The pumps are calibrated within the experimental system by measuring weight of the pumped liquid using a digital scale (MyWeigh, model iBALANCE i1200). The two pumps used in this experiment deliver the identical volumetric flow rate of 40 ml min^{-1} through conduits of the identical size, thus, the foulant stream average velocities are equal between the two flow systems. However, due to difference in control sequences, we observe two significantly different instantaneous velocity profiles. We inject air bubbles into the flow system conduits and use high speed cameras (Photron, model FASTCAM Mini AX200) to monitor the instantaneous velocity of the foulant stream. We observe the differences in both the magnitude of the instantaneous velocity, and the duration of the displacement cycle period. Most notably, the programmable control pump experiences a 0.1 s flow reversal every period caused by the pump's intermittent rest; liquid rebounds from the rollers' sudden stop. The change in flow direction, and the greater pumping cycle frequency for the programmable control pump flow system imply the longer particle residence time in the vicinity of the fibre. However, we are not able to demonstrate any discernible trends in terms of measured OD_{600} values between the two systems. The differences in particle residence time and the differences in the instantaneous velocity profiles do not critically affect the probability of TiO_2 particle attachment. Similar behaviour is observed in the case of biofouling, where immobile microorganisms crucially rely on the presence of flow to be able to attach to a structure and start the proliferation [33–37]. Pump flow profiles and the demarcation of measurements for each pumping system are provided in electronic supplementary material, figures S4 and S5.

Flow profiles in the vicinity of the fibres are determined by a computational fluid dynamics (CFD) simulation using the Autodesk CFD software suite and assume unidirectional flow only. The three-dimensional model geometry is discretized into a tetrahedral cell mesh, with a resolution of 20 cells per feature. Both mesh and equation discretization orders are first order, which is deemed suitable for our application: non-transient bulk flow, with relatively simple geometry, low velocity and pressure, and no moving parts or shock events. The boundary layer is described by three wall layers, with a layer height multiplication factor of 1.2. The final height of each layer is then determined by multiplying the local isotropic length scale for the wall surface by the layer factor [59]. Wall roughness of the fibre is approximated as the mean arithmetic roughness of the human hair, R_a = 1 µm [60], which is not dissimilar to the apparent roughness of the animal fibres as measured on the SEM images from §4. In the absence of a manufacturer's specification, wall roughness of PLA surfaces is taken as a conservative value

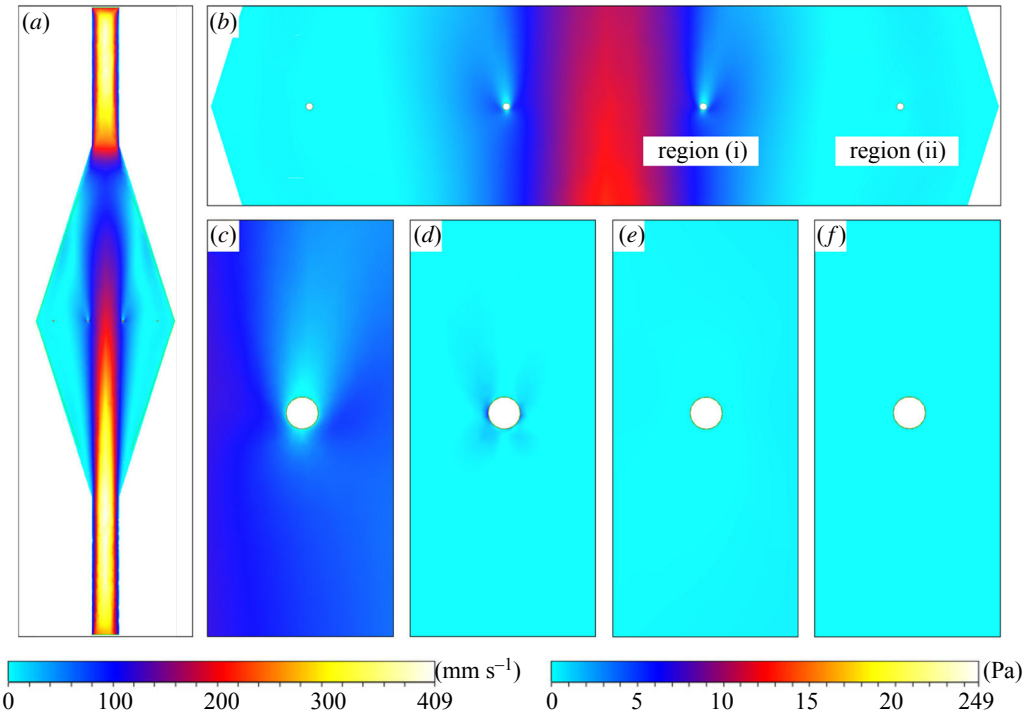

Figure 3. Selected heat map views of the CFD simulation results. (*a*) Cross-sectional overview of the velocity field in the mounting connector. (*b–c*) Cross-sectional views of the foulant stream across the fibres. (*b*) Enlarged view of the fibres, local velocity heat map and directional vectors. (*c–f*) Enlarged heat map views for individual fibres, left to right: (*c*) velocity, (*d*) shear stress for the fibres next to the long axis, and (*e*) velocity, (*f*) shear stress for the fibres in the stagnant corner zones. Flow direction is from top to bottom. Velocity magnitude scale bar is shown on the bottom left, shear stress magnitude scale bar on the bottom right.

of $R_a = 1$ µm, based on the data available in the literature [61]. Boundary conditions are set with a volumetric flow rate of 40 ml min^{-1} at the inlet, and relative static pressure of 0 Pa at the outlet. A converging solution is obtained by automated mesh adaptation, through an initial and three additional simulation cycles, where the number of cycles is determined by the approach to full independence of the solution from the mesh. Solution independence from the mesh reached 99.92% for bulk pressure and 99.33% for bulk velocity. CFD results are presented in figure 3. We observe two distinct flow profiles around the fibres: unidirectional uniform flow across the two fibres closer to the long axis—region (i)—and the near-stagnant, circulating backflow in the two corner zones—region (ii). The simulated velocity profile around the fibre, figure 3*c*, reveals the anticipated laminar flow without separation, but also the near zero velocity condition outside of the flow core. The surface shear stress on the fibre, shown in figure 3*d*, reaches the value of 4.9 Pa. The two fibres located in the stagnant parts of the liquid volume outside the core, are exposed to effectively no velocity and shear stress. We observe significantly reduced flow velocities near all fibres, in both locations, however the causes for flow slowing down are fundamentally different. Fibres near the centre of the conduit obstruct the flow causing the friction and inertial deceleration in the thin boundary layer, while the fibres at the far ends experience a simple deceleration of the flow due to the increase in net free flow area. The differences between regions (i) and (ii) is evident from the comparison of wall shear stress profiles (figure 3*d*,*f*).

2.3. Fouling experiments

Water is circulated in a closed-loop flow system for 24 h, exposing four fibres of the same type to the foulant stream. Each type of fibre is tested at least three times, where *n* is the number of tests. Fur strands are cut at one end using a separate, clean surgical blade. The other end of the hair is detached together with the adhesive using the forceps. The portion of the sample that is exposed to the flow is then separated using curved stainless steel scissors. In case of the latex coupons, the edges are trimmed using the surgical blade to eliminate adhesive contamination. The samples are then placed in a semi-micro 3 ml cuvette (BrandTech), filled with 1 ml of distilled water to completely cover the samples. An adjustable volume pipette dispenser (Fisherbrand, model Elite) is used to transfer liquid.

The cuvette is sealed using a custom-made PLA lid and placed in the ultrasonic cleaner (ISONIC). A fabricated PLA holder keeps the cuvette in an upright position in the middle of the bath filled with distilled water. The bath water level is kept higher than the level of liquid in the cuvette but below the cuvette's top edge to prevent bath water ingress. A cleaning cycle is selected as recommended by the manufacturer for the case of an enclosed container in the bath. Typical fur samples before and after cleaning are shown in figure 4. Following cleaning, the cuvette is removed from the ultrasonic bath using the forceps and dried with Kimwipes. Another cuvette, filled with distilled water but holding no samples, is used for spectrometer blanking. Once the blank reading is taken, the cuvette holding ultrasonically cleaned samples is placed in the spectrophotometer. At least 20 consecutive readings are taken for each set of samples.

3. Experimental results

We expose individual synthetic fibres, and fur strands from three terrestrial mammal orders and three semi-aquatic mammal orders to a pulsatile colloid flow carrying TiO_2 particles. An overview of mean OD_{600} values as measured in our

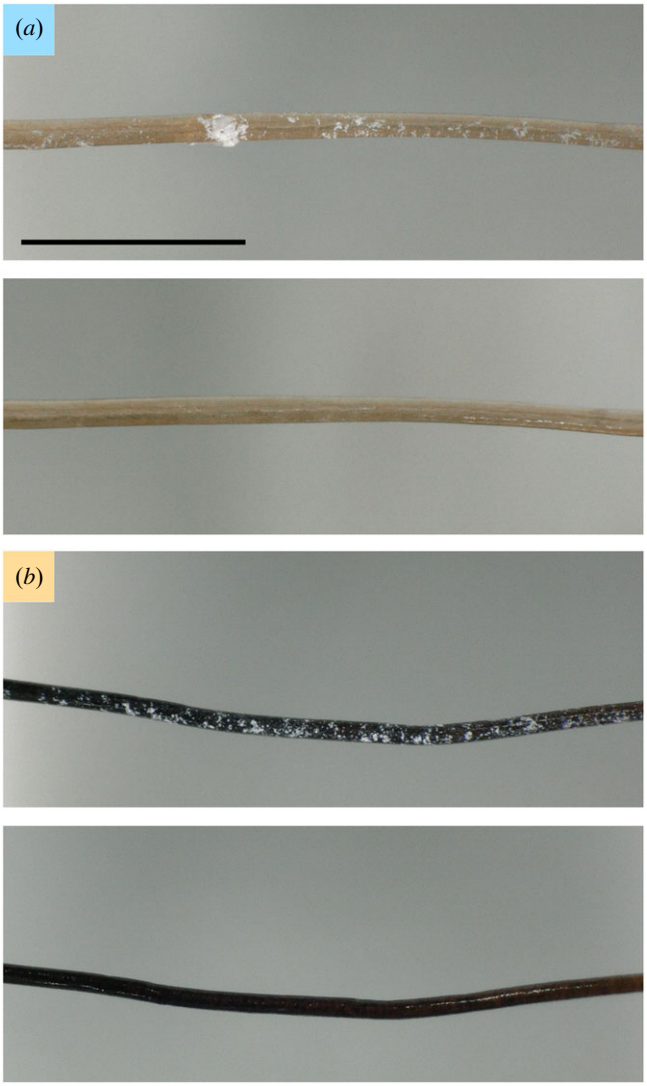

Figure 4. Fouled fibres before and after ultrasonic cleaning. (*a*) American beaver fur and (*b*) coyote fur. Scale bar represents 1 mm and is common for all panels.

tests is presented in table 1. Control trials performed without TiO_2 present for PP, beaver and coyote strands produced OD_{600} values that are functionally zero. Distilled water control trials indicate that TiO_2-rich flow OD_{600} readings indeed originate from the TiO_2 particles, and not from the impurities in the flow system.

We estimate a Reynolds number for flow over a 100 µm circular cylinder to be $Re_D = \rho UD/\mu \approx 10$, indicating laminar flow with two attached standing eddies [62]. Here, ρ is the density of liquid, U is the bulk flow velocity, D is the diameter of filament and μ is the dynamic viscosity of water. Approximating the average-sized clump of TiO_2 as a sphere, our estimate for the mean Stokes number is $St = \rho_p D_p^2 U/(18\,\mu l) \approx 0.0015$, with $St < 0.1$ for more than 99.9% of the TiO_2 clumps, which indicates that the particles faithfully follow the instantaneous velocity field. Here, ρ_p is the density of TiO_2, D_p is the diameter of clump and L is the characteristic dimension—in this case, the diameter of a hair fibre.

The OD_{600} readings are translated into numbers of attached TiO_2 particles, N_p, using the fit curve defined in equation (2.1). Considering that removal of the particles from the hair in the ultrasonic cleaner is comprehensive, N_p represents the ability of the fibre to attract and retain particles during the fouling process. As evident from table 1, fibres in region (ii) attract more particles, the latex fibre being an exception. Latex and muskox fibres are the outliers in the flow and the near-quiescent liquid groups, respectively, attracting significantly more particles than other fibres. Different instantaneous velocity profiles of the two pumps—discussed in §2.2, and depicted in electronic supplementary material, figures S4 and S5—produced a consistent total number of attached particles, N_p, between the two pumping systems, and over the period of 24 h. The consistent results indicate that long-term exposure to particles outweighs any short-term effects of the pumps' instantaneous velocity profile.

The value of N_p ignores the significant difference in average diameters of experimental fibres and thus, the surface area exposed to the foulant stream. Therefore, we reduce the total number of particles, N_p, by the surface area in contact with the foulant stream, A_S, to obtain the surface-normalized number of arrested particles, N_p^*, as a measure of the anti-fouling performance of an individual fibre. We calculate A_S using the average diameter of the fibre, $\bar{D}$ and the cumulative length of the fibres, L, as: $A_S = \bar{D}\pi L$. The means of N_p and N_p^* are presented in table 1 and the full distribution in figure 5. Our reading of surface-normalized values N_p^* suggests that the anti-fouling performance of a fibre is not a characteristic inherent to a class of fibres, as evident from table 1.

In order to carry out a more rigorous comparison and establish the degree of correlation between the fibre samples, we perform a Kruskal–Wallis statistical test, a one-way analysis of variance on ranks. Our statistical approach is chosen because the samples are independent and the normality assumption cannot be verified. Our study reveals statistically significant differences between the fibres with respect to the normalized number of attached TiO_2 particles, both in region (i), $\chi^2 = 352.273$, $p = 0.000$ and region (ii), $\chi^2 = 382.907$, $p = 0.000$. However, we also observe pairs of fibres from different groups exhibiting significant similarities in the anti-fouling performance. Fibres exhibiting a high degree of agreement in N_p^* include beaver–muskox ($p = 0.772$), springbok–sea otter ($p = 0.0669$) and coyote–muskrat ($p = 0.202$) fibre pairs in flow, and polypropylene–sea otter ($p = 0.800$), coyote–muskrat ($p = 0.677$) and springbok–muskox ($p = 0.325$) fibre pairs for the near-quiescent environment. Therefore, statistical analysis confirms similarity of behaviour between different groups as suggested by the tabulated data.

Due to the absence of the distinction in anti-fouling behaviour between different fibre materials we turn our attention to shape. Latex, tested in filamentous form, also offers the opportunity to be tested in the planar form. We expose latex coupons to liquid in the two disparate regimes—flow and near-quiescent. We establish the fouling intensity performance in relation to two seemingly obvious cardinal number candidates: exposed surface area of the samples A_S, and the Reynolds number Re_D in case of fibres, or Re_L in case of coupons. The results, as shown in figure 6*a*,*b*, indicate that coupons foul more than fibres in both flow environments. However, the flat samples' apparent trendline changes the sign of the slope between the two plots. The increase in A_S is expected to facilitate deposition [11], but we find that fouling intensity does not strongly correlate with absolute surface area exposed for all types of samples. This includes both flat and cylindrical specimens. Surprisingly, for a given surface area, neither class of fibre shows any

Table 1. Experimental fibre types and fouling metrics.

group	material	hydraulic diameter (μm)	OD_{600}, TiO_2	OD_{600}, clean water	$\bar{N}_p$, 10^6 (—)	$\bar{N}_p^*$, 10^{13} (m^{-1})
flow—two fibres in region (i) and two in region (ii)						
synthetic fibres	polypropylene	84.7	0.041	0.004	112.9 ($n = 3$)	4.422
	latex	208.7	0.192	—	454.9 ($n = 3$)	7.055
semi-aquatic mammals	sea otter	47.8	0.029	—	86.3 ($n = 4$)	5.516
	beaver	118.3	0.052	0.003	139.0 ($n = 4$)	3.796
	muskrat	70.8	0.055	—	146.0 ($n = 3$)	6.662
terrestrial mammals	springbok	82.9	0.051	—	136.2 ($n = 4$)	5.468
	muskox	115.6	0.055	—	145.4 ($n = 4$)	3.869
	coyote	109.6	0.092	0.006	231.4 ($n = 4$)	6.755
near-quiescent—two fibres mounted in region (ii)						
synthetic fibres	polypropylene	91.2	0.104	—	256.9 ($n = 3$)	9.440
	latex	198.2	0.049	—	132.3 ($n = 4$)	2.305
semi-aquatic mammals	sea otter	57.6	0.053	—	142.2 ($n = 4$)	9.318
	beaver	128.0	0.080	—	203.8 ($n = 4$)	5.437
	muskrat	82.4	0.063	—	164.5 ($n = 3$)	7.563
terrestrial mammals	springbok	88.2	0.117	—	287.3 ($n = 3$)	10.953
	muskox	141.3	0.206	—	484.2 ($n = 3$)	17.299
	coyote	113.1	0.096	—	239.0 ($n = 4$)	7.256

correlation in fouling intensity with Reynold's number. However, it is clear that flat topography is more prone to foul under flow. Such results highlight the complex interactions between factors affecting the deposition, as noted in §1, and indicate that N_p^* is governed by more than one parameter.

We repeat the correlation analysis for all fibre materials, and for the variety of the cardinal variables related to the properties of the samples and the flow: exposed surface area of the samples A_S, fibre scale length L_S, scale projected ridge length L_R, curvature radius $1/R$, and Reynolds numbers Re_D and Re_L. We present the plots in the electronic supplementary material. This extended analysis again shows inconsistent trends when N_p^* is correlated to the individual properties. Between different body shape, surface topography and flow parameters, there is no individual factor dominantly guiding the anti-fouling performance of the fibres.

The fouling of fibres is heavily dependent on the presence of flow, as described in §3 and shown in figure 5. For example, latex fibres exposed to flow foul approximately 3.1 × more compared to the fibres in region (ii) alone. Therefore, the two fibres located in region (i) must attract proportionally more particles per surface area, N_p^*, for the measurements to result in mean values as depicted on figure 5*b*. The anti-fouling performance further deteriorates in case of flat coupons that experience the same absence of flow and wall shear stresses as the two remote fibres.

4. Analysis of results with dimensionless groups

In order to understand the interactions of a variety of flow- and shape-related factors affecting the deposition, we employ the Buckingham-Π theorem to establish dimensionless groups from cardinal variables. We consider the following flow and shape parameters as relevant to the particle deposition on a wetted filamentous object

- N_p^*, the surface-normalized number of attached particles;
- $1/R$, surface curvature radius;
- t, cumulative time of sample exposure to the foulant stream;
- c, concentration of particles in the liquid;
- U, bulk velocity upstream of the fibre;
- μ, dynamic viscosity;
- ρ, liquid density;
- $\emptyset$, non-dimensional circularity parameter;
- ϵ, non-dimensional surface features factor;
- τ_w, surface shear stress.

Surface curvature radius, $1/R$, is selected not only to describe the roundness of the surface but also as a proxy for the exposed surface area A_S which, as previously noted, is expected to have a positive correlation with the independent parameter N_p^*. Time t and the concentration of the particles c are two additional factors expected to maintain a similar trend. We consider the bulk velocity of the foulant stream U together with the physical properties of the liquid, μ and ρ, to account for momentum. In order to simplify the complex influence of the various factors, U is restricted to two discrete values, as explained in §2, while t and c are kept constant in our experiments. Such an approach allows us to focus on the characteristics of fibres and the interactions in the vicinity of the surface.

Typically, a scaling analysis will assume an identical, circular, cross-sectional shape across different length scales, which is not true in the case of natural fibres. Fibre cross-sections are non-circular, and vary significantly between different fibre

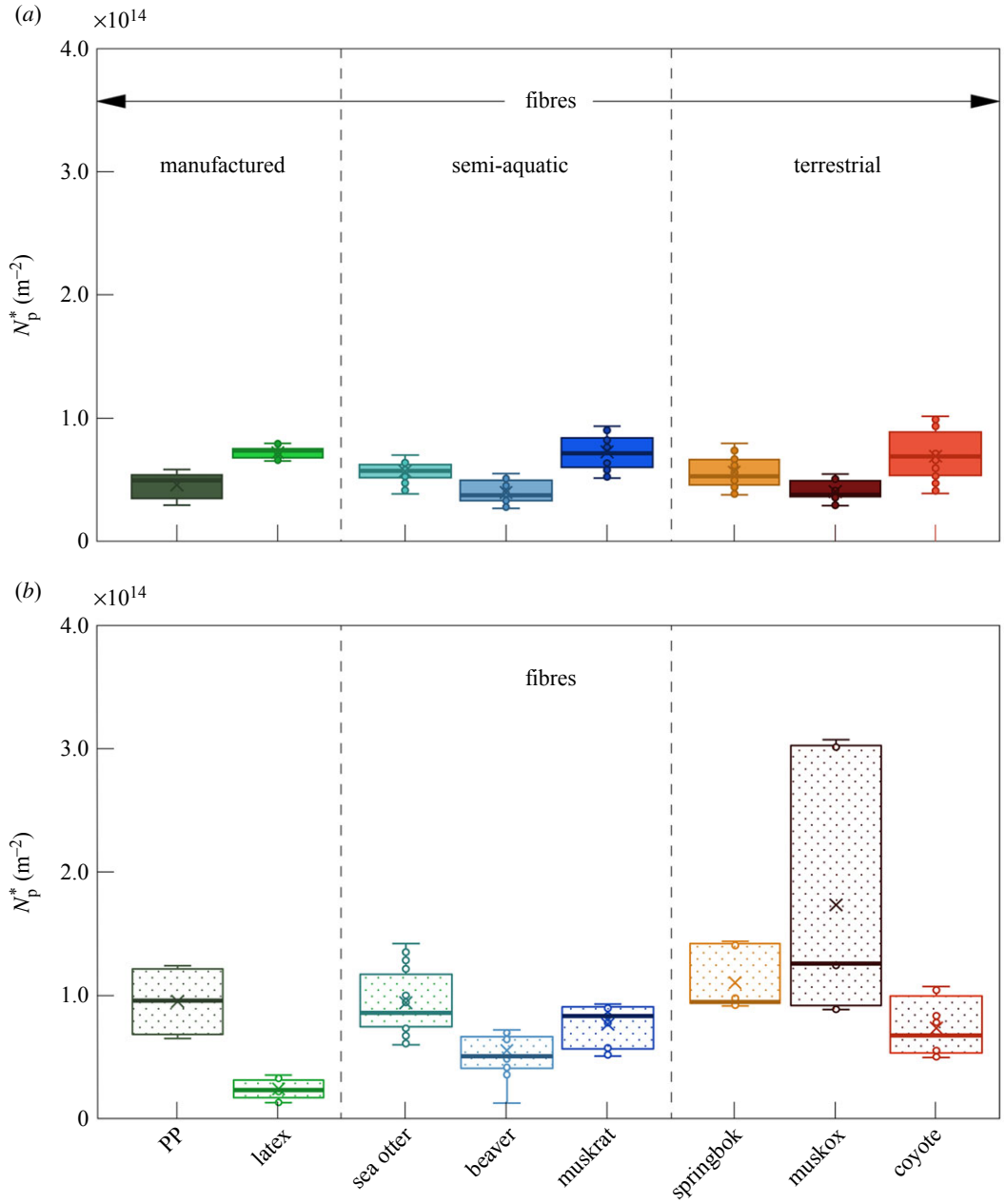

Figure 5. Surface-normalized number of attached TiO_2 particles, N_p^*, per sample type: (*a*) in flow and (*b*) in near-quiescent liquid.

types as shown in figure 1. In order to account for the deviation from the circular cross-sectional shape, we introduce the non-dimensional circularity parameter, ø. Circularity is defined as: $= 4\pi A/P^2$, where A is the cross-sectional area and P is the perimeter length of the cross-section. An overview of circularity for different fibres is given in figure 7.

A radial view of an average fibre, figure 8, reveals insignificant protrusion length of surface scales when compared with the diameter of the fibre, the length of the scale ridges L_R and the scale length L_S. The conventional definition of surface roughness as the mean deviation of the profile or contour [63] is typically used to determine the friction factor and accompanying flow drag across curved surfaces [64]. In the case of the animal hair, the scales' low profile and similarity in height across various fibres do not permit such differentiation between the species. Furthermore, the description of friction by means of the one-dimensional surface roughness factor does not describe the unique profile of scales and ridges or the different fur types. Fibre surface features aiding the lodging of particles are therefore more accurately described by the length and the density of the crevices formed by hair scales. We describe unique features of the crevices via the non-dimensional ratio $\epsilon = L_S \cdot L_R / A_U$, where A_U represents the fibre surface projected unit area.

The remaining parameter, wall shear stress τ_w, is selected to describe the behaviour of flow in the vicinity of the surface and the influence of the boundary layer [11]. To estimate the magnitude of τ_w, we use the potential flow velocity components [65]

$$u_r = \left[1 - \frac{R^2}{r^2}\right] U \cos(\theta),$$
$$u_\theta = -\left[1 + \frac{R^2}{r^2}\right] U \sin(\theta),$$
$$\tau_w = \mu \left[r \frac{\partial}{\partial r}\left(\frac{u\theta}{r}\right) + \frac{1}{r}\frac{\partial u_r}{\partial \theta}\right] = \frac{4}{R}\mu U \sin(\theta). \qquad (4.1)$$

Parameters ρ, U and $1/R$ have units comprised of the three primary dimensions: mass, length or time, and cannot be combined into another non-dimensional parameter—

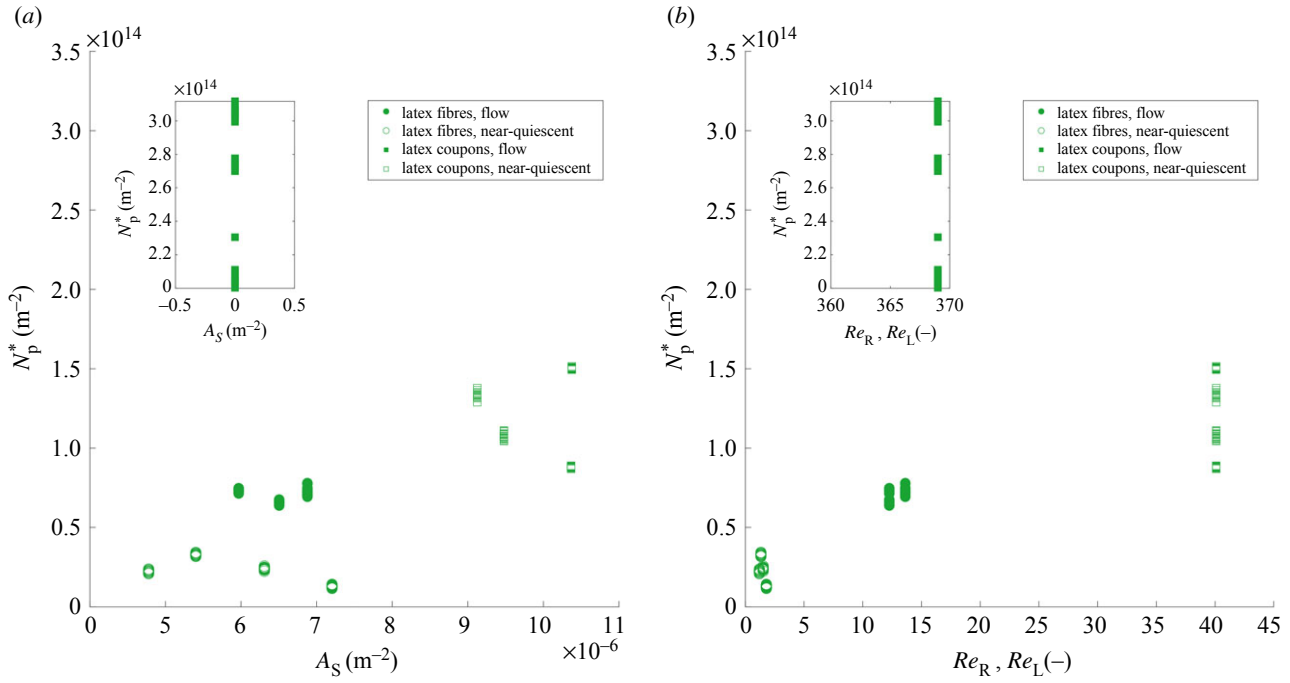

Figure 6. Latex samples surface-normalized number of attached TiO_2 particles, N_p^*, in relation to (*a*) exposed sample area A_S and (*b*) Reynolds number Re_D.

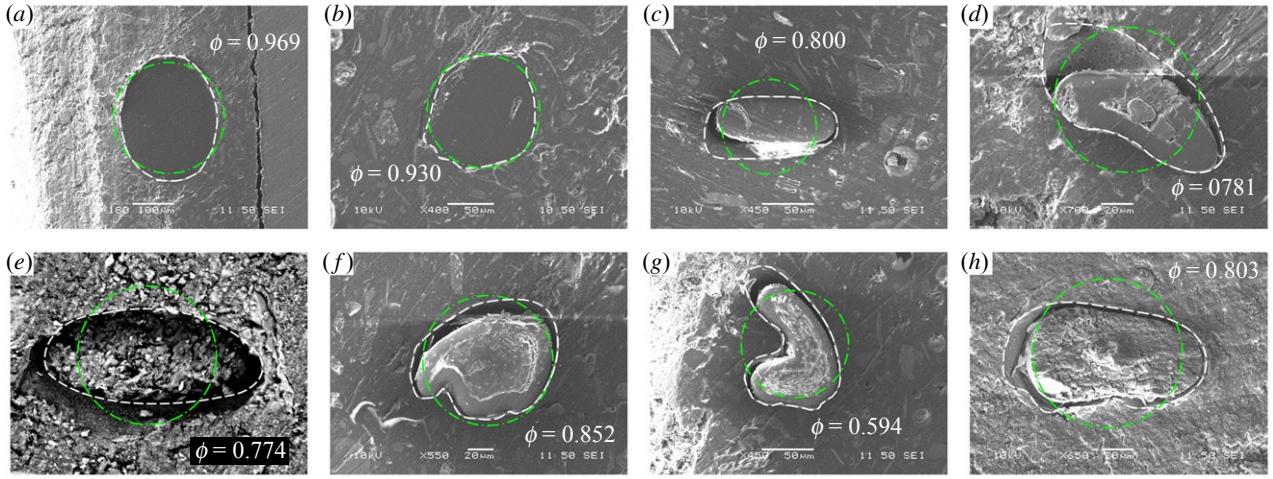

Figure 7. Examples of fibre circularity parameter Ø. (*a–b*) Synthetic fibres: (*a*) polypropylene monofilament, (*b*) latex coated polypropylene monofilament. (*c–e*) Semi-aquatic mammals: (*c*) American beaver, (*d*) muskrat, (*e*) sea otter. (*f –h*) Terrestrial mammals: (*f*) coyote, (*g*) springbok, (*h*) muskox. The white line follows the shape of the fibre as embedded in the epoxy resin. The green line represents the circle of the same cross-sectional area *A* as the area enclosed by the white line.

therefore, we consider them as repeating parameters. We derive the general form of Π-terms equation

$$N_p^*\left(\frac{1}{R}\right)^{-2} = f\left[\frac{1}{Re_R}, U\left(\frac{1}{R}\right)t, \frac{c}{\left(\frac{1}{R}\right)^3}, \emptyset, \epsilon, \frac{\tau_w}{\rho U^2}\right], \tag{4.2}$$

Next, we anticipate the fouling intensity trend for a change in each contributing non-dimensional parameter. For the parameters as listed in equation (4.2), we predict that N_p^* increases with the increase in: μ, t, c, $\emptyset$, ϵ and τ_W, and decreases with the rise of: ρ, U and R. Distributing the variables based on this prediction, we propose the relationship

$$\underbrace{N_p^* \cdot \left(\frac{1}{R}\right)^{-2}}_{\Gamma} \sim \underbrace{Re_R\left(\frac{1}{R}\right)^{-2} \emptyset\epsilon\left(\frac{\tau_w}{\rho U}\right)tc}_{\Pi_T}. \tag{4.3}$$

such that,

$$\Gamma \sim \Pi_T. \tag{4.4}$$

The plots of non-dimensional term Γ are presented in figures 9 and 10. Bivariate correlation statistical test shows a strong positive relationship for the results obtained in the near-quiescent liquid region, region (ii), $r(560) = 0.751$, $\sim p = 0.000$, and the results obtained for the flowing region, region (i), if the latex outlier is excluded, $r(520) = 0.716$, $p = 0.000$. The correlation for the complete set of samples in region (i) is weak, as expected by looking at the plot, with negative slope and significantly low weight, $r(580) = -0.210$,

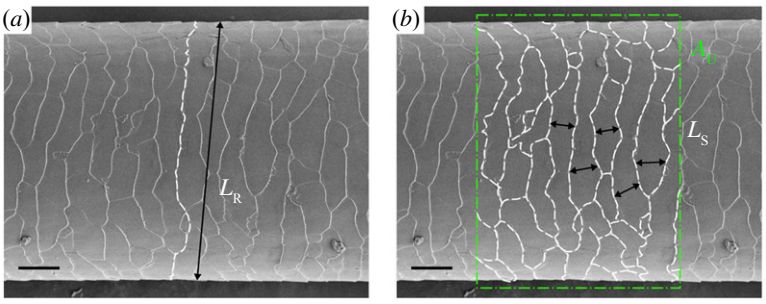

Figure 8. Non-dimensional roughness parameter ϵ, shown here on the example of coyote fur. (*a*) Scale ridge projected length, L_R. (*b*) Average distance between the ridges is defined by scale length, L_S, highlighted here for fibre projected unit area A_U, 1 mm long. L_R is shown as white dashed line. A_U of the fibre is outlined by green centreline. Scale bar represents 20 µm.

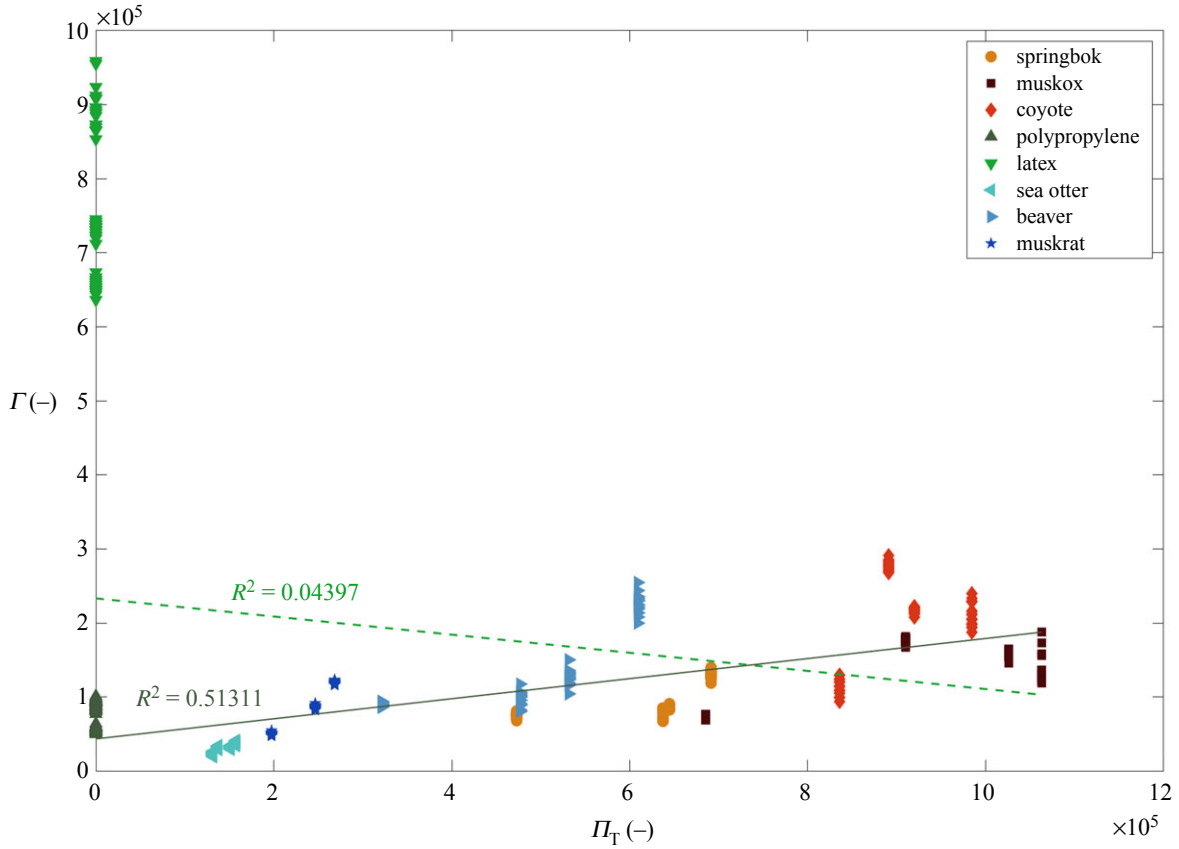

Figure 9. Non-dimensional Π-term correlation for fibres in region (i). The dashed line designates the trendline for the complete set of samples, while the solid line shows the trend for fibres sans latex.

$\sim p = 0.000$. It is apparent that fouling of latex fibre is flow-dependent, and that anti-fouling performance degrades as the flow accelerates. When natural fibres alone are considered, the correlations are: $r(460) = 0.747$, $p = 0.000$, for region (i), and $r(420) = 0.863$, $p = 0.000$, for region (ii).

5. Discussion and conclusion

Submerged fibres of synthetic and natural origin exhibit similar anti-fouling behaviour when exposed to a suspension of inorganic particles. This absence of anti-fouling trends is maintained for the different flow regimes. The averages of the total number of attached particles $\bar{N}_p$ and the surface normalized number of the attached particles $\bar{N}_p^*$ (table 1) indicate no inherent differences in susceptibility to fouling between the different fibre groups. The results raise a question if the anti-fouling behaviour of fur is a targeted evolutionary advantage. Tropical and arctic animals alike grow fur that provides approximately the same thermal insulation coverage per body surface area [66] which suggests that insulation is one of the main factors driving the evolution of fur. Resistance to fouling, as anecdotally observed in nature, may simply be a fortuitous by-product inherent to fur morphology, rather than a targeted characteristic unique to any specific mammalian order.

The deposition of particles carried by a liquid is governed by a plethora of factors and their complex interactions, some of which are still unknown. The results presented in §3 corroborate such a notion, and indicate strong positive correlations between fouling intensity characterized by a non-dimensional parameter Γ, which incorporates: the flow regime, sample exposure time, concentration of particles in the liquid, sample area, circularity shape factor, roughness factor and viscous

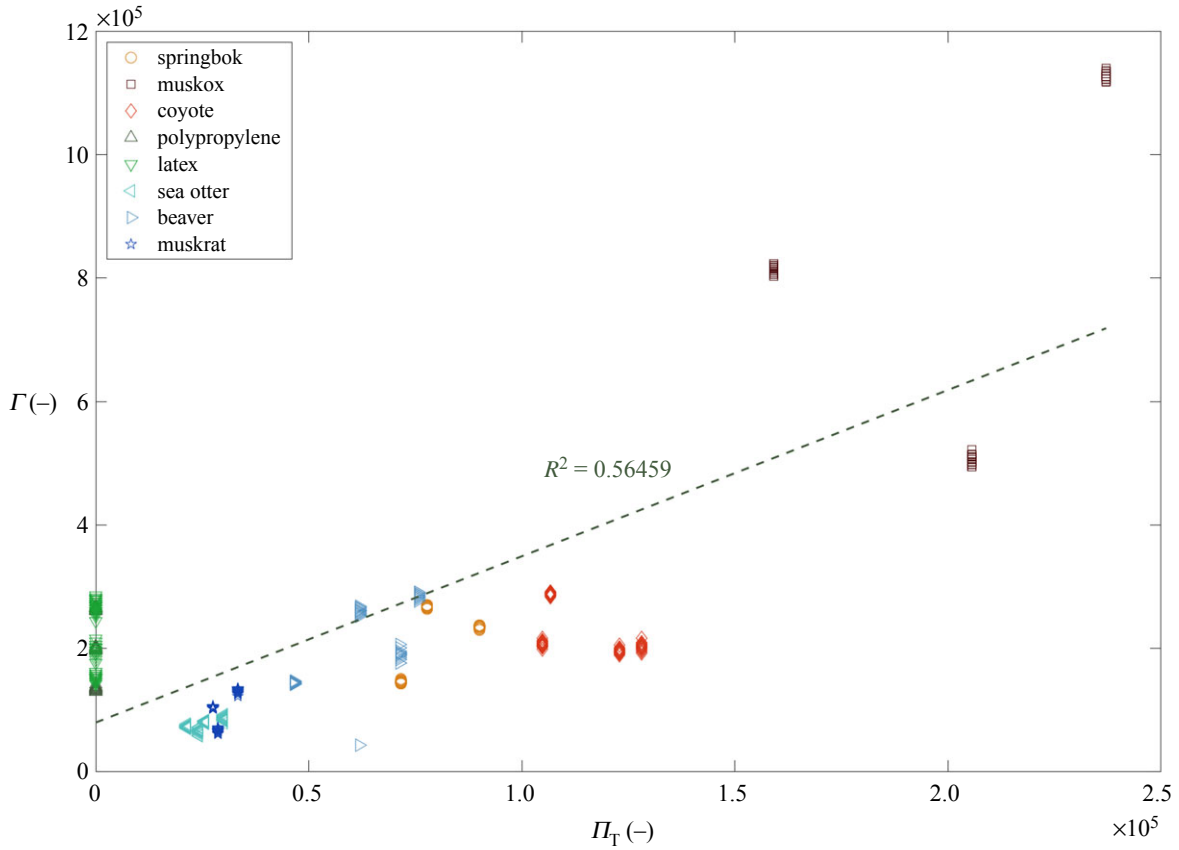

Figure 10. Non-dimensional Π-terms correlation for fibres in region (ii). The dashed line designates the trendline for the complete set of samples.

shear stress at the surface, characterized by a non-dimensional parameter Π_T. No individual form or flow factor appears to dominate $\bar{N}_p^*$, as shown in electronic supplementary material, figures S6–S23. However, the non-dimensionalized combination of factors presented in equation (4.3) reveals a strong correlation between Γ and Π_T for both flow regimes, with the exception of the clear outlier, the latex fibre in flow. Our tests with latex confirm the findings that latex has extraordinary susceptibility to fouling [52], albeit we show that the susceptibility is strongly affected by the flow regime of the surrounding suspension. The effect of flow on anti-fouling behaviour is evident in the comparison of the effects of Π_T on Γ between the two flow conditions, figures 9 and 10. An increase in Π_T of several orders of magnitude for the moving suspension produces a similar fouling intensity to that of the near-static environment, and even then, the rate of change of Γ with Π_T is noticeably slower in flow. Estimates of the average river velocities [67] indicate that a fur-like filament in a river is exposed to two adjacent tiers of flow regimes: $Re_D < 40$, the laminar flow with attached vortices, as studied in this work, or $40 < Re_D < 60$–100, the transitional flow between laminar and turbulent regime characterized by the so-called von Kármán vortex street [62]. Thus, semi-aquatic animals face a choice between increased fur fouling in quiet waters and cleaner fur at the expense of an increased energy expenditure required to endure fiercer currents. The fur of terrestrial mammals exhibits the same anti-fouling behaviour as the fur of semi-aquatic mammals, figures 9 and 10. The terrestrial mammal samples we tested represent animals inhabiting diverse landscapes and experiencing various degrees of water exposure: from arid environments to climates with heavy rain and snow. It is highly unlikely for the anti-fouling properties of fur to, at the same time, be the main evolutionary target of a follicle's development, and remain so consistent across vastly different climates. Finally, we note that contrary to all the individual factors, shown in the electronic supplementary material, figures S6–S23, it is only the $\Gamma - \Pi_T$ relationship that shows a demarcation between the semi-aquatic and the terrestrial furs (figures 9 and 10).

In our experiments, we focus on factors that allow us to carry out non-dimensional parameters analysis such as flow, fibre shape and surface topography, rather than chemical, biological, surface or other interactions. We further reduce the complexity of interactions of the different factors by fixing the type of the foulant, time period t, concentration c, volumetric flow rate Q, and liquid properties μ and ρ to a single or only a couple of discrete values. However, our non-dimensional parameter analysis is unable to capture all the aforementioned complex factors and their interactions, such as surface forces, for example. The outlier case of latex fibres may be a result of a synergistic effect of such an additional factor, the effect being amplified in flow. The comparison between latex fibres and coupons suggests that flat surfaces foul more than the filamentous structures, at least in case of one material. Again, it is not clear if this behaviour is due to surface interactions, shape factor or some other factor. The combined effects that the different surface, chemical or even biological interactions may have on our results present an opportunity for future investigations.

The experiments presented here are carried out on taut fibres fixed at both ends, in an effort to limit the already significant number of individual variables affecting fouling. The natural behaviour of fur anchored only at one end is such that the tip can move freely, and can do so in concert with surrounding strands. Simple models of flexing scale-covered filaments indicate that particle attachment rate varies based

on a change in radius, and the direction of the fibre curvature [18]. On the macroscopic level, hair strands rub against each other in flow and during locomotion, thus imposing mechanical stresses across the surface of the fibres which we expect to at least partially remove deposited foulants. Very dense pelts of some semi-aquatic mammals maintain a layer of air adjacent to the skin during swimming. Trapped air drastically reduces the heat transfer [68,69], and also renders the inner layers of fur less hospitable or inaccessible to potential foulers. It is known that hair-like randomly patterned surfaces reduce the drag [70], which in turn, improves the anti-fouling characteristics of the stratum exposed to flow [12]. Our experiments are conducted on singular furs and it is possible that aggregate anti-fouling is enhanced by the flow in ways not captured by this study. The absence of distinctions in anti-fouling between natural and synthetic fibres, or between the tested natural fibres alone, suggests that simple slenderness may dominate fur's anti-fouling characteristics, or that by limiting deformation we have muted more complex variable interactions. It is not yet fully known how multiple phenomena combine to govern the fouling of a flexing aggregated structure, and is a fertile area for future work. Specifically, fibres anchored at an attack angle other than 90°, fibres anchored at only one end, and fibre aggregates deserve investigation.

In this study, we provide a foundation for understanding of fur anti-fouling behaviour. Our study is based on consideration of factors limited in number to control the daunting complexity of natural systems. Fur anti-fouling behaviour presents an enticing research opportunity, with anticipated practical benefits. Nature has developed a plethora of mechanisms to combat fouling [12]. Anti-fouling strategies include self-cleaning surfaces, hydrophobicity, chemical secretions, bacteria message manipulation in flora, micro-textured skin, drag reduction and flexion of scales, hydrophobic feathers, wax coatings, and mushroom-shaped spines found in fauna, and eyelid wipers and red blood cell phospholipid membranes in humans. Mammalian fur appears to have its own anti-fouling mechanisms, which may work in concert, but it is not yet known how such mechanisms function. Human-developed anti-fouling techniques typically rely on either active, energy consuming measures: contact pressure, steam, hot air, radiation, ultrasonic and ultraviolet light sterilization, or chemical treatment, such as the use of toxins and disinfectants [12]. Understanding the passive mechanism of fur anti-fouling could permit its replication in the form of surfaces, structures, or coatings lacking the drawbacks of the current cleaning methods.

Data accessibility. The data are provided in electronic supplementary material [71]. Experimental data are available in perpetuity via Open Science Framework: https://osf.io/v7he8/.

Authors' contributions. M.K.: conceptualization, data curation, formal analysis, investigation, methodology, project administration, resources, software, validation, visualization, writing—original draft, writing—review and editing; H.A.: formal analysis, writing—review and editing; D.B.: data curation, investigation, methodology, writing—original draft; R.G.: conceptualization, investigation, methodology, supervision, validation, writing—original draft; A.K.D.: formal analysis, funding acquisition, resources, supervision, validation, writing original draft, writing—review and editing.

All authors gave final approval for publication and agreed to be held accountable for the work performed therein.

Competing interests. We declare we have no competing interests.

Funding. The authors acknowledge the National Science Foundation (CMMI-1825801) for funding this work.

Acknowledgements. The authors would like to thank Dr Charissa de Bekker for lending laboratory equipment and consumable supplies, Peter Schmitt of Textile Development Associates, Inc. for supplying polypropylene monofilaments and Dr Michael Kinzel for helpful discussions on CFD simulation.

References

1. Bott TR. 1995 *Fouling of heat exchangers*. Amsterdam, The Netherlands: Elsevier.
2. Shan L, Fan H, Guo H, Ji S, Zhang G. 2016 Natural organic matter fouling behaviors on superwetting nanofiltration membranes. *Water Res.* **93**, 121–132. (doi:10.1016/j.watres.2016.01.054)
3. Hellio C, Yebra D. 2009 *Advances in marine antifouling coatings and technologies*. Boca Raton, FL: CRC Press.
4. Jermann D, Pronk W, Boller M. 2008 Mutual influences between natural organic matter and inorganic particles and their combined effect on ultrafiltration membrane fouling. *Environ. Sci. Technol.* **42**, 9129–9136. (doi:10.1021/es800654p)
5. Gwon E-m, Yu M-j, Oh H-k, Ylee Y-h. 2003 Fouling characteristics of NF and RO operated for removal of dissolved matter from groundwater. *Water Res.* **37**, 2989–2997. (doi:10.1016/S0043-1354(02)00563-8)
6. Badal D, Jayarani AV, Kollaran MA, Kumar A, Singh V. 2020 *Pseudomonas aeruginosa* biofilm formation on endotracheal tubes requires multiple two-component systems. *J. Med. Microbiol.* **69**, jmm001199. (doi:10.1099/jmm.0.001199)
7. Chan J, Wong S. 2010 *Biofouling: types, impact and anti-fouling*. New York, NY: Nova Science Publishers.
8. Fabbri S *et al.* 2017 Fluid-driven interfacial instabilities and turbulence in bacterial biofilms. *Environ. Microbiol.* **19**, 4417–4431. (doi:10.1111/1462-2920.13883)
9. Camper AK, McFeters GA. 2000 Problems of biofouling in drinking water systems. In *Industrial biofouling: detection, prevention and control* (eds J Walker, S Surman, J Jass), pp. 15–38. New York, NY: John Wiley & Sons Ltd.
10. Gordon DP, Mawatari SF. 1992 *Atlas of marine-fouling Bryozoa of New Zealand ports and harbours*. Miscellaneous Publication. Wellington, New Zealand: New Zealand Oceanographic Institute.
11. Melo L, Bott TR, Bernardo CA. 2012 *Fouling science and technology*. Series E: Applied Sciences vol. 145. Dordrecht, The Netherlands: Kluwer Academic Publishers.
12. Bixler GD, Bhushan B. 2012 Biofouling: lessons from nature. *Phil. Trans. R. Soc. A* **370**, 2381–2417. (doi:10.1098/rsta.2011.0502)
13. Edwards SJ, Kjellerup BV. 2013 Applications of biofilms in bioremediation and biotransformation of persistent organic pollutants, pharmaceuticals/personal care products, and heavy metals. *Appl. Microbiol. Biotechnol.* **97**, 9909–9921. (doi:10.1007/s00253-013-5216-z)
14. Singh R, Paul D, Jain RK. 2006 Biofilms: implications in bioremediation. *Trends Microbiol.* **14**, 389–397. (doi:10.1016/j.tim.2006.07.001)
15. Wimpenny J, Manz W, Szewzyk U. 2000 Heterogeneity in biofilms. *FEMS Microbiol. Rev.* **24**, 661–671. (doi:10.1111/j.1574-6976.2000.tb00565.x)
16. Tian L, Ahmadi G, Wang Z, Hopke PK. 2012 Transport and deposition of ellipsoidal fibers in low reynolds number flows. *J. Aerosol Sci.* **45**, 1–18. (doi:10.1016/j.jaerosci.2011.09.001)
17. Lin W, Shi R, Lin J. 2021 Distribution and deposition of cylindrical nanoparticles in a turbulent pipe flow. *Appl. Sci.* **11**, 962. (doi:10.3390/app11030962)
18. Krsmanovic M, Biswas D, Ali H, Kumar A, Ghosh R, Dickerson AK. 2020 Hydrodynamics and surface properties influence biofilm proliferation. *Adv. Colloid Interface Sci.* **288**, 102336. (doi:10.1016/j.cis.2020.102336)
19. Yebra DM, Kiil S, Dam-Johansen K. 2004 Antifouling technology—past, present and future steps towards efficient and environmentally friendly antifouling coatings. *Prog. Org. Coat.* **50**, 75–104. (doi:10.1016/j.porgcoat.2003.06.001)

20. Fusetani N. 2004 Biofouling and antifouling. *Nat. Prod. Rep.* **21**, 94–104. (doi:10.1039/b302231p)
21. Flemming H-C, Griebe T, Schaule G. 1996 Antifouling strategies in technical systems-a short review. *Water Sci. Technol.* **34**, 517–524. (doi:10.2166/wst.1996.0591)
22. Asuri P, Karajanagi SS, Kane RS, Dordick JS. 2007 Polymer–nanotube–enzyme composites as active antifouling films. *Small* **3**, 50–53. (doi:10.1002/smll.200600312)
23. Olsen SM, Pedersen LT, Laursen MH, Kiil S, Dam-Johansen K. 2007 Enzyme-based antifouling coatings: a review. *Biofouling* **23**, 369–383. (doi:10.1080/08927010701566384)
24. Satheesh S, Ba-akdah MA, Al-Sofyani AA. 2016 Natural antifouling compound production by microbes associated with marine macroorganisms: a review. *Electron. J. Biotechnol.* **19**, 26–35. (doi:10.1016/j.ejbt.2016.02.002)
25. Wang K-L, Wu Z-H, Wang Y, Wang C-Y, Xu Y. 2017 Mini-review: antifouling natural products from marine microorganisms and their synthetic analogs. *Marine Drugs* **15**, 266. (doi:10.3390/md15090266)
26. Wan F, Ye Q, Yu B, Pei X, Zhou F. 2013 Multiscale hairy surfaces for nearly perfect marine antibiofouling. *J. Mater. Chem. B* **1**, 3599–3606. (doi:10.1039/c3tb20545b)
27. Patenaude F, Bovet J. 1984 Self-grooming and social grooming in the north american beaver, castor canadensis. *Can. J. Zool.* **62**, 1872–1878. (doi:10.1139/z84-273)
28. Allen SG, Stephenson M, Risebrough RW, Fancher L, Shiller A, Smith D. 1993 Red-pelaged harbor seals of the san francisco bay region. *J. Mammal.* **74**, 588–593. (doi:10.2307/1382277)
29. Bentall GB, Rosen BH, Kunz JM, Miller MA, Saunders GW, LaRoche NL. 2016 Characterization of the putatively introduced red alga *Acrochaetium secundatum* (Acrochaetiales, Rhodophyta) growing epizoically on the pelage of southern sea otters (*Enhydra lutris nereis*). *Mar. Mammal Sci.* **32**, 753–764. (doi:10.1111/mms.12275)
30. Lewin RA, Robinson PT. 1979 The greening of polar bears in zoos. *Nature* **278**, 445–447. (doi:10.1038/278445a0)
31. Lewin RA, Farnsworth PA, Yamanaka G. 1981 The algae of green polar bears. *Phycologia* **20**, 303–314. (doi:10.2216/i0031-8884-20-3-303.1)
32. Sokolov VE, Sokolov VE. 1982 *Mammal skin*. Berkeley, CA: University of California Press.
33. Korber DR, Lawrence JR, Sutton B, Caldwell DE. 1989 Effect of laminar flow velocity on the kinetics of surface recolonization by Mot^+ and Mot^- *Ppseudomonas fluorescens*. *Microb. Ecol.* **18**, 1–19. (doi:10.1007/BF02011692)
34. Scheuerman TR, Camper AK, Hamilton MA. 1998 Effects of substratum topography on bacterial adhesion. *J. Colloid Interface Sci.* **208**, 23–33. (doi:10.1006/jcis.1998.5717)
35. Evans LV. 2003 *Biofilms: recent advances in their study and control*. New York, NY: CRC Press.
36. Kim MK, Drescher K, Pak OS, Bassler BL, Stone HA. 2014 Filaments in curved streamlines: rapid formation of *Staphylococcus aureus* biofilm streamers. *New J. Phys.* **16**, 065024. (doi:10.1088/1367-2630/16/6/065024)
37. Wheeler JD, Secchi E, Rusconi R, Stocker R. 2019 Not just going with the flow: the effects of fluid flow on bacteria and plankton. *Annu. Rev. Cell Dev. Biol.* **35**, 213–237. (doi:10.1146/annurev-cellbio-100818-125119)
38. Merritt PM, Danhorn T, Fuqua C. 2007 Motility and chemotaxis in *Agrobacterium tumefaciens* surface attachment and biofilm formation. *J. Bacteriol.* **189**, 8005–8014. (doi:10.1128/JB.00566-07)
39. Graham MV, Mosier AP, Kiehl TR, Kaloyeros AE, Cady NC. 2013 Development of antifouling surfaces to reduce bacterial attachment. *Soft Matter* **9**, 6235–6244. (doi:10.1039/c3sm50584g)
40. Cheng Y, Feng G, Moraru CI. 2019 Micro- and nanotopography sensitive bacterial attachment mechanisms: a review. *Front. Microbiol.* **10**, 191. (doi:10.3389/fmicb.2019.00191)
41. Finlay JA, Schultz MP, Cone G, Callow ME, Callow JA. 2013 A novel biofilm channel for evaluating the adhesion of diatoms to non-biocidal coatings. *Biofouling* **29**, 401–411. (doi:10.1080/08927014.2013.777046)
42. Schumacher JF *et al.* 2007 Engineered antifouling microtopographies—effect of feature size, geometry, and roughness on settlement of zoospores of the green alga *Ulva*. *Biofouling* **23**, 55–62. (doi:10.1080/08927010601136957)
43. An R, Dong Y, Zhu J, Rao C. 2017 Adhesion and friction forces in biofouling attachments to nanotube- and peg-patterned TiO_2 surfaces. *Colloids Surf., B* **159**, 108–117. (doi:10.1016/j.colsurfb.2017.07.067)
44. Mafu AA, Roy D, Goulet J, Magny P. 1990 Attachment of *Listeria monocytogenes* to stainless steel, glass, polypropylene, and rubber surfaces after short contact times. *J. Food Prot.* **53**, 742–746. (doi:10.4315/0362-028X-53.9.742)
45. Lindner E. 1992 A low surface free energy approach in the control of marine biofouling. *Biofouling* **6**, 193–205. (doi:10.1080/08927019209386222)
46. Zhao Q, Liu C, Liu Y, Wang S. 2007 Bacterial and protein adhesion on NI-P-PTFE coated surfaces. In *Proc. 7th Int. Conf. on Heat Exchanger Fouling and Cleaning: Challenges and Opportunities 2007. Heat Exchanger Fouling and Cleaning VII ECI Symposium Series, vol. RP5. Tomar, Portugal 1-6 July 2007*. See http://toc.proceedings.com/05181webtoc.pdf.
47. Dexter SC, Sullivan JD, Williams J III, Watson SW. 1975 Influence of substrate wettability on the attachment of marine bacteria to various surfaces. *Appl. Environ. Microbiol.* **30**, 298–308. (doi:10.1128/am.30.2.298-308.1975)
48. Akesso L *et al.* 2009 Deposition parameters to improve the fouling-release properties of thin siloxane coatings prepared by PACVD. *Appl. Surf. Sci.* **255**, 6508–6514. (doi:10.1016/j.apsusc.2009.02.032)
49. Navabpour P, Teer D, Su X, Liu C, Wang S, Zhao Q, Donik C, Kocijan A, Jenko M. 2010 Optimisation of the properties of siloxane coatings as anti-biofouling coatings: comparison of PACVD and hybrid PACVD–PVD coatings. *Surf. Coat. Technol.* **204**, 3188–3195. (doi:10.1016/j.surfcoat.2010.03.011)
50. Tsibouklis J, Stone M, Thorpe AA, Graham P, Nevell TG, Ewen RJ. 2000 Inhibiting bacterial adhesion onto surfaces: the non-stick coating approach. *Int. J. Adhes. Adhes.* **20**, 91–96. (doi:10.1016/S0143-7496(99)00034-2)
51. Dickerson AK, Mills ZG, Hu DL. 2012 Wet mammals shake at tuned frequencies to dry. *J. R. Soc. Interface* **9**, 3208–3218. (doi:10.1098/rsif.2012.0429)
52. Rogers J, Dowsett AB, Dennis PJ, Lee JV, Keevil CW. 1994 Influence of plumbing materials on biofilm formation and growth of *Legionella pneumophila* in potable water systems. *Appl. Environ. Microbiol.* **60**, 1842–1851. (doi:10.1128/aem.60.6.1842-1851.1994)
53. Biswas D, Casey DM, Crowder DC, Steinman DA, Yun YH, Loth F. 2016 Characterization of transition to turbulence for blood in a straight pipe under steady flow conditions. *J. Biomech. Eng.* **138**, 071001. (doi:10.1115/1.4033474)
54. Pantai USA Inc. 620 Titanium dioxide product information. See https://www.pantaiusa.com/product-page/pantai-ptr-620-titanium-dioxide-tio2-1-lb (accessed 29 January 2022).
55. Winkler J. 2014 *Titanium dioxide*. Hannover, Germany: Vincentz Network.
56. Shi H, Magaye R, Castranova V, Zhao J. 2013 Titanium dioxide nanoparticles: a review of current toxicological data. *Particle Fibre Toxicol.* **10**, 1–33. (doi:10.1186/1743-8977-10-1)
57. Xu G, Zhang J, Li G, Song G. 2003 Effect of complexation on the zeta potential of titanium dioxide dispersions. *J. Dispersion Sci. Technol.* **24**, 527–535. (doi:10.1081/DIS-120021807)
58. Geiss O *et al.* 2021 Particle size analysis of pristine food-grade titanium dioxide and e 171 in confectionery products: interlaboratory testing of a single-particle inductively coupled plasma mass spectrometry screening method and confirmation with transmission electron microscopy. *Food Control* **120**, 107550. (doi:10.1016/j.foodcont.2020.107550)
59. Autodesk. Wall layers cfd 2019 Autodesk knowledge network.html. See https://knowledge.autodesk.com/support/cfd/learn-explore/caas/CloudHelp/cloudhelp/2019/ENU/SimCFD-UsersGuide/files/GUID-F9C4DDB4-8111-4F25-8EDE-D7C38B3BAD99-htm.html (accessed 2 February 2022).
60. Park KH, Kim HJ, Oh B, Lee E, Ha J. 2018 Assessment of hair surface roughness using quantitative image analysis. *Skin Res. Technol.* **24**, 80–84. (doi:10.1111/srt.12393)
61. Liu W, Zhou J, Ma Y, Wang J, Xu J. 2017 Fabrication of pla filaments and its printable performance. In *IOP Conf. Series: Materials Science and Engineering*, vol. 275, p. 012033. IOP Publishing.
62. Panton RL. 2006 *Incompressible flow*. New York, NY: John Wiley & Sons.
63. DeGarmo EP, Black JT, Kohser RA, Klamecki BE. 1997 *Materials and process in manufacturing*. Upper Saddle River, NJ: Prentice Hall.
64. Moody LF. 1944 Friction factors for pipe flow. *Trans. ASME* **66**, 671–684.

65. White FM, Majdalani J. 2006 *Viscous fluid flow*, **vol. 3**. New York, NY: McGraw-Hill.
66. Scholander PF, Walters V, Hock R, Irving L. 1950 Body insulation of some arctic and tropical mammals and birds. *Biol. Bull.* **99**, 225–236. (doi:10.2307/1538740)
67. Schulze K, Hunger M, Döll P. 2005 Simulating river flow velocity on global scale. *Adv. Geosci.* **5**, 133–136. (doi:10.5194/adgeo-5-133-2005)
68. Liwanag HEM, Berta A, Costa DP, Abney M, Williams TM. 2012 Morphological and thermal properties of mammalian insulation: the evolution of fur for aquatic living. *Biol. J. Linnean Soc.* **106**, 926–939. (doi:10.1111/j.1095-8312.2012.01900.x)
69. Fish FE, Smelstoys J, Baudinette RV, Reynolds PS. 2002 Fur does not fly, it floats: buoyancy of pelage in semi-aquatic mammals. *Aquatic Mammals* **28**, 103–112.
70. Itoh M, Tamano S, Iguchi R, Yokota K, Akino N, Hino R, Kubo S. 2006 Turbulent drag reduction by the seal fur surface. *Phys. Fluids* **18**, 065102. (doi:10.1063/1.2204849)
71. Krsmanovic M, Ali H, Biswas D, Ghosh R, Dickerson AK. 2022 Fouling of mammalian hair fibres exposed to a titanium dioxide colloidal suspension. Figshare.